

AD-755 219

**HIGH-EFFICIENCY, SINGLE-FREQUENCY LASER
AND MODULATOR STUDY**

Robert C. Ohlmann, et al

Lockheed Missiles and Space Company

Prepared for:

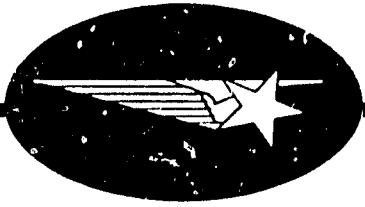
**Office of Naval Research
Advanced Research Projects Agency**

30 November 1972

DISTRIBUTED BY:



**National Technical Information Service
U. S. DEPARTMENT OF COMMERCE
5285 Port Royal Road, Springfield Va. 22151**



AD 755219

L

This document has been approved
for public release and sale; its
distribution is unlimited.

D D C
REPRODUCED
REGULARLY
FEB 5 1973
B

Reproduced by
**NATIONAL TECHNICAL
INFORMATION SERVICE**
U S Department of Commerce
Springfield VA 22151

HIGH-EFFICIENCY, SINGLE-FREQUENCY LASER
AND MODULATOR STUDY

7th Quarterly Summary Technical
Status Report

N-JY-71-14

30 November 1972

R. C. Ohlmann, W. Culshaw, K. K. Chow, H. V. Hance,
W. B. Leonard, and J. Kannelaud

ARPA Order No. 306

Contract No. N00014-71-C-0049

Program Code 421

Effective Date of Contract: 1 September 1970

Expiration Date: 31 October 1972

Amount: \$284,900

Scientific Officer:

Director, Physics Programs
Physical Sciences Division

Office of Naval Research, Arlington, Va. 22217

R. C. Ohlmann (415) 493-4411, ext. 45275

Principal Investigator:

Sponsored by the

Advanced Research Projects Agency

ARPA Order No. 306

The views and conclusions contained in this document are those of the authors and should not be interpreted as necessarily representing the official policies, either expressed or implied, of the Advanced Research Projects Agency or the U.S. Government.

Lockheed Palo Alto Research Laboratory
LOCKHEED MISSILES & SPACE COMPANY, INC.
A Subsidiary of Lockheed Aircraft Corporation
Palo Alto, California 94304

This document has been approved
for public release and sale; its
distribution is unlimited.

D D C
REF ID: A
FEB 5 1973
B

CONTENTS

Section	Page
ILLUSTRATIONS	iii
TABLES	iv
1 INTRODUCTION	1-1
1.1 Objectives	1-1
1.2 Efficient Single-Frequency Nd:YAG Lasers	1-1
1.3 Wide-Bandwidth Electrooptical Modulator	1-2
2 EFFICIENT SINGLE-FREQUENCY Nd:YAG LASER STUDIES	2-1
2.1 Basic LMSC Laser Cavity Design Studies	2-1
2.2 Tilted Fabry-Perot Etalon and Metallic Film Mode Selector	2-5
2.2.1 Mode Filter Design and Frequency Response	2-5
2.2.2 Discussion of Mode Filter Performance	2-7
2.2.3 Use of a Convex Mirror R_1	2-11
2.2.4 Use of a Curved Mirror R_2	2-11
2.2.5 Etalon Loss in Highly Focused Laser Cavities	2-14
2.2.6 Conclusions	2-17
2.3 Double-Intracavity Etalon Mode Filter	2-17
2.4 Plans for Next Quarter	2-19
3 WIDE BANDWIDTH ELECTROOPTICAL MODULATOR	3-1
3.1 Measurement Techniques for 2- to 4-GHz Modulator	3-1
3.2 Modulation Tests	3-9
3.3 Future Plans	3-17

ILLUSTRATIONS

Figure		Page
2-1	Use of Laser Rod as Intracavity Focusing Lens With Appropriate Curvatures R on Rod	2-2
2-2	Beam Spot Radius at the YAG Rod Versus Curved Mirror-Rod Distance d_1 for Various Mirror Radii R_1 and Focal Lengths of the Laser Rod	2-3
2-3	Beam Waist Radius Versus Curved Mirror Distance d_1 for Various Values of Curved Mirror Radius R_1	2-4
2-4	Combination of the Tilted Fabry-Perot Etalon and the Single Metallic-Film Multilayer Reflector for Single-Frequency Operation of Nd:YAG Lasers	2-6
2-5	Frequency Response for an 11-mm, 38-Percent Reflective Quartz Fabry-Perot Etalon and a 2-mm, 64 A Nichrome Film-Laser Mirror Quartz Etalon	2-8
2-6	Selectivity Curves for an 11-mm Fabry-Perot Etalon With Various Reflective Multilayer Coatings	2-9
2-7	Threshold Pump Power of Nd:YAG Laser Versus Intracavity Fabry-Perot Etalon Tilt Angle for an 11-mm Quartz Etalon with 35-Percent Reflective Coatings	2-15
2-8	Flat Laser Mirror Replaced by a Curved Mirror	2-16
2-9	Double Intracavity Fabry-Perot Etalon Mode Filter for the Single-Frequency Operation of Nd:YAG Lasers	2-18
3-2	Modulation Index Versus Frequency for Various rf Drive Levels	3-10
3-3	Modulation Index Versus Frequency at 5-W rf Level	3-11
3-4	Modulation Index Versus Frequency With rf Power Flow in the Reverse Direction	3-13
3-5	Modulation Index Versus Frequency at Various Power Levels, Calculated From the Sideband of the Extraordinary Ray Only	3-14
3-6	Modulation Index Versus Frequency for 8-mm LiNbO_3 Crystal Using the Birefringent Sideband Measurement	3-15
3-7	Actual rf Drive Power into the Modulator as a Function of Frequency	3-16

TABLES

Table	Page
2-1 Beam Spot Radius W_R at the YAG Rod and Beam Waist W_D for Mirror Radius R_1 of r and 10 CM	2-1
2-2 Beam Spot Radius W_R at the YAG for Convex Mirror Radius R_1 of 5 and 10 CM	2-11
2-3 Beam Spot Radius at the YAG Rod and Beam Waist for Various Curved Laser Mirror Radii R_1 and R_2	2-13

Section 1

INTRODUCTION

1.1 OBJECTIVES

The general objective of this research and development program is to conduct investigations that will contribute to the development of an ultrawide-bandwidth laser communication system. The specific objectives are:

- (1) A study of laser communication system configurations, particularly modulation formats, that are most suitable for very high data rates up to 2 Gbit/sec
- (2) Research on high-efficiency, single-frequency Nd:YAG lasers as the transmitter source for such a communication system
- (3) Research on an optical modulator with 2 GHz of rf bandwidth and good modulation efficiency

The primary emphasis of the program is on objectives (2) and (3). However, a considerable amount of work on the first objective, the study of optical communication modulation formats, has also been done. The results, together with our recommendations on the choice of modulation format, were presented in depth in the Second Semi-annual Technical Report and this part of the task is essentially completed. During the present reporting period, work has continued on improving the efficiency and ease of single-frequency operation of Nd:YAG lasers, together with work on the extension of the bandwidth of the optical modulator.

1.2 EFFICIENT SINGLE-FREQUENCY Nd:YAG LASERS

The main effort in this development since the last technical report has been directed towards the elimination of the critical behavior encountered with the tilted Fabry-Perot etalon and metallic mode filter, particularly in highly efficient laser cavities with tight focusing designed to produce adequate TEM_{00} mode volumes in the laser rod.

A substantial improvement in the overall stability and ease of adjustment of the single-frequency laser has been accomplished by the replacement of the metallic film by a second thin intracavity dielectric etalon of low reflectivity. This performs the same function as the metallic film; i.e., it eliminates oscillations at other free spectral ranges of the other main selective Fabry-Perot etalon, but is more easily adjusted to give stable single-frequency operation in these more efficient and tightly focused Nd:YAG laser cavity configurations.

1.3 WIDE-BANDWIDTH ELECTROOPTICAL MODULATOR

During this reporting period, additional theoretical work on the sideband-power measurement techniques was done to relate modulation index to sideband power. Such an analysis is necessary because there is currently no photodetector that has a flat response to 4 GHz.

Modulation tests using 8-mm LiNbO₃ crystals were also conducted at 0.6328 and 0.5145 μm . Results obtained so far indicate that the crystal may be too long for the modulator. Nevertheless, tests made at 5-W rf drive level at the output of the TWT (corresponding to a drive of about 4 W at the input to the modulator) gave approximately 30-percent modulation depth across the 2- to 4-GHz band. These results correlated well with the earlier measurements at 0.6328 μm and gave confidence in scaling the performance for 1.06- μm operation.

Section 2
EFFICIENT SINGLE-FREQUENCY Nd:YAG LASER STUDIES

2.1 BASIC LMSC LASER CAVITY DESIGN STUDIES

The laser cavity developed for the efficient use of the population inversion in the pumped Nd:YAG rod is shown in Fig. 2-1. Here the rod is radiused as shown to act as an intracavity focusing lens which, together with a short-radius concave mirror R_1 , allows the attainment of optimum TEM_{00} mode volumes within the pumped rod. Some computed values of the spot radius W_R at the rod and the beam waist radius between mirror R_1 and the rod are shown in Figs. 2-2 and 2-3. A value of $d_2 = 20$ cm was used in these computations, but the results are relatively independent of this distance which is determined by the dimensions of the efficient spherical pumping cavity used in practice. Table 2-1 gives some values of these parameters at the center of the stability range of d_1 .

Table 2-1
BEAM SPOT RADIUS W_R AT THE YAG ROD AND BEAM WAIST W_D
FOR MIRROR RADIUS R_1 OF 5 AND 10 CM

(All dimensions in cm; curved rod radius $R = 25$ cm)

<u>R_1</u>	<u>d_1</u>	<u>d_2</u>	<u>W_R</u>	<u>W_D</u>
5	32.6	20	0.111	0.0092
10	35.0	20	0.079	0.0130

W_R and W_D are relatively independent of the distance d_2 , and the stable region of d_1 extends from $d_1 = f$ to $d_1 = f + R_1$, where $f = R/(n - 1)$ is the focal length of the curved rod, and n is the refractive index of YAG.

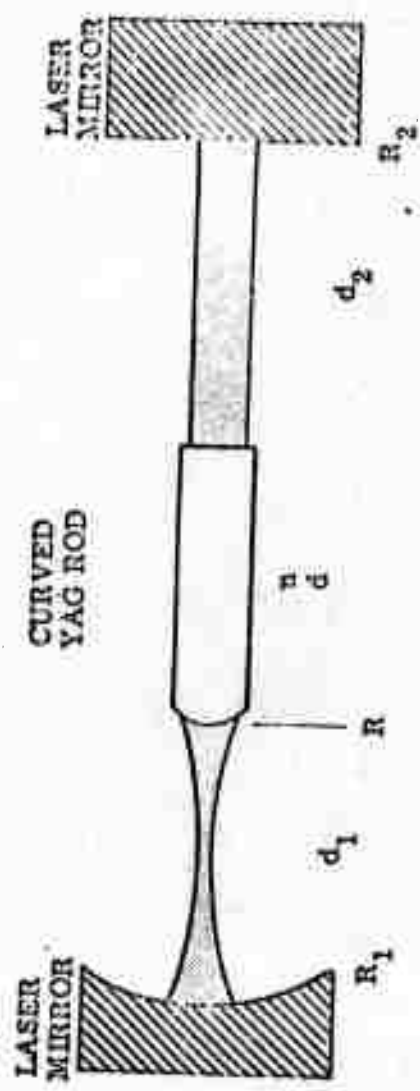
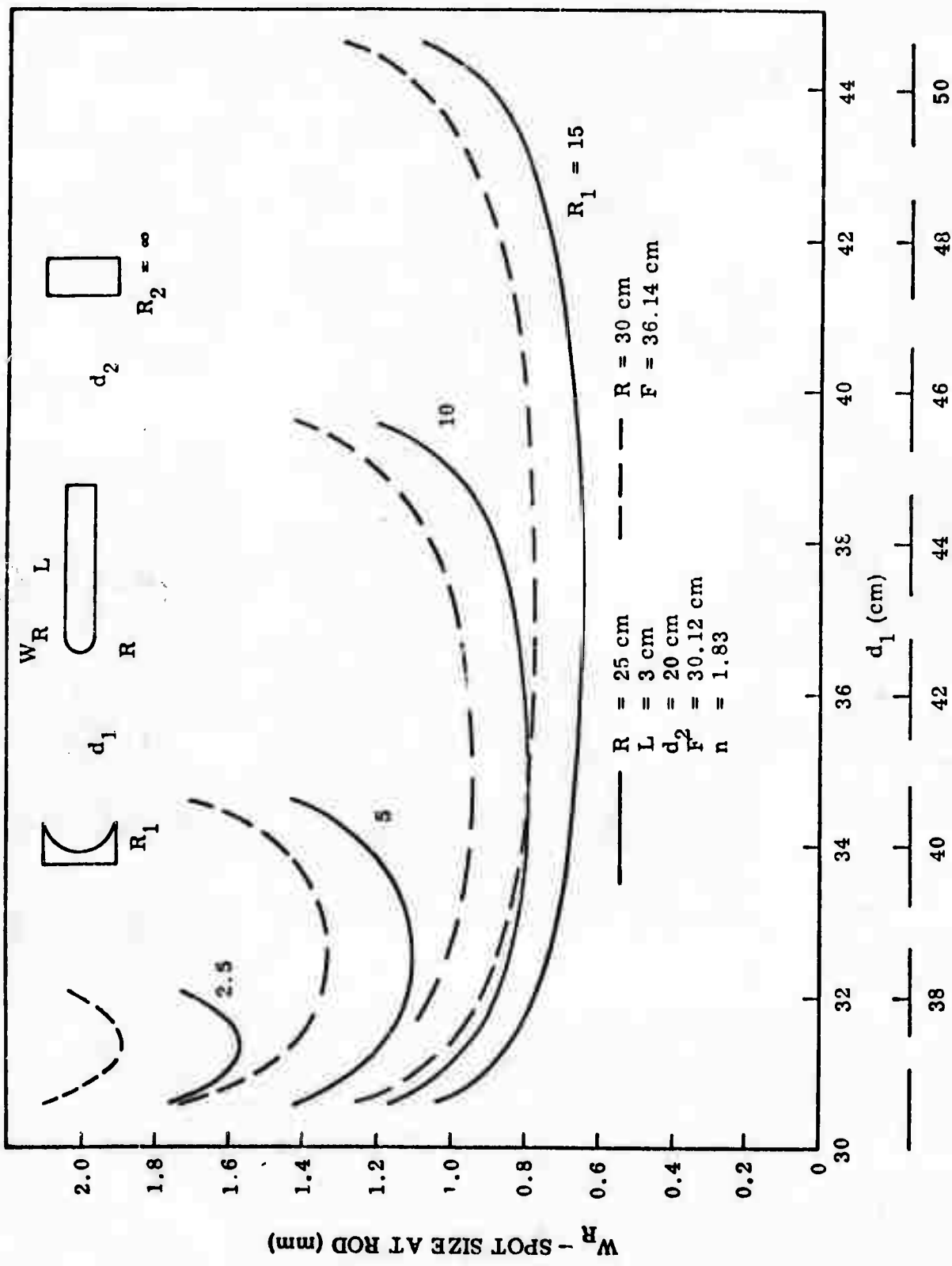


Fig. 2-1 Use of Laser Rod as Intracavity Focusing Lens With
Appropriate Curvatures R on Rod



2-3

Fig. 2-2 Beam Spot Radius at the YAG Rod Versus Curved Mirror-Rod Distance d_1 for Various Mirror Radii R_1 and Focal Lengths of the Laser Rod

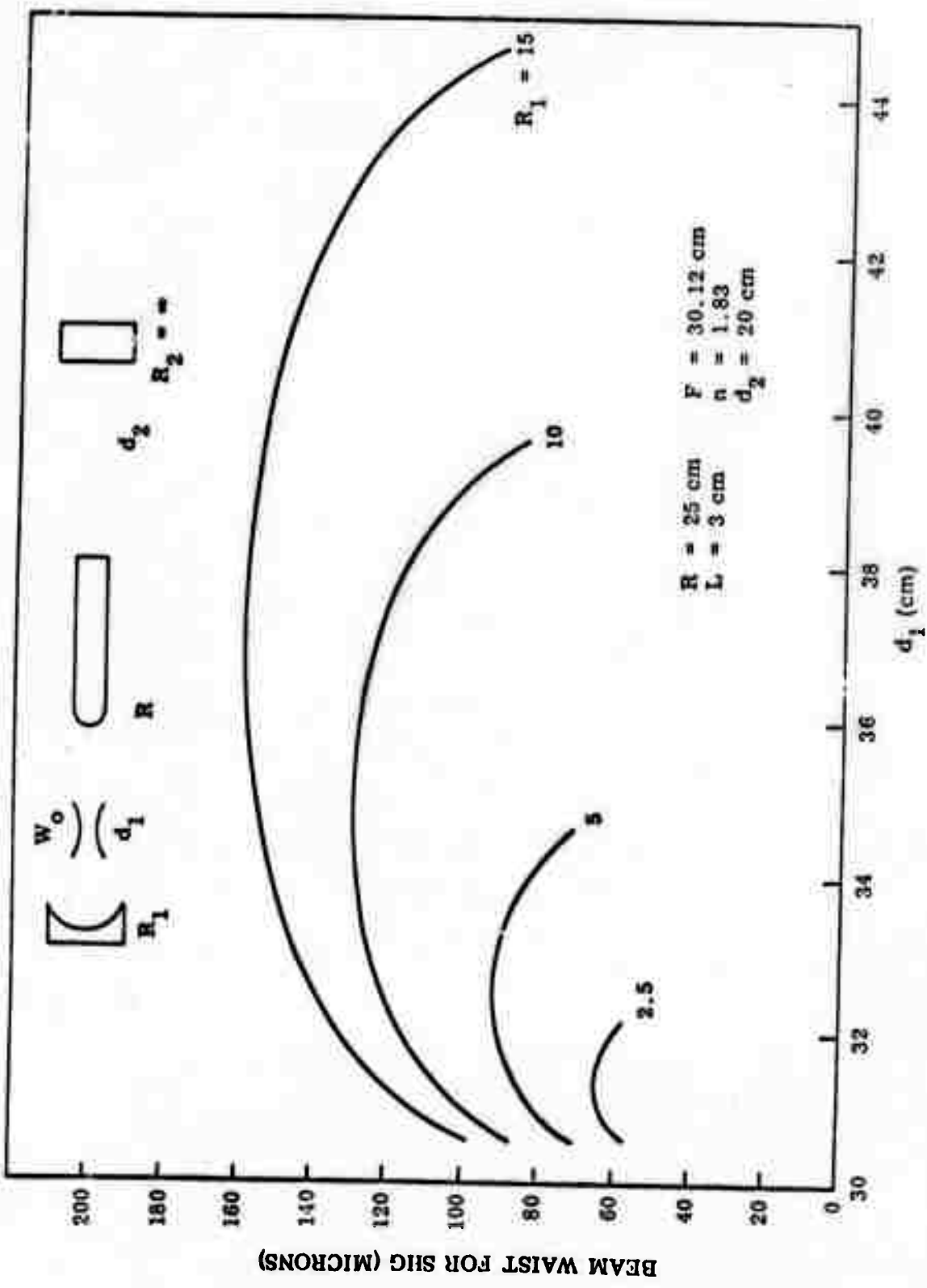


Fig. 2-3 Beam Waist Radius Versus Curved Mirror Distance d_1 for Various Values of Curved Mirror Radius R_1

Such cavity designs thus allow an adequate filling of the YAG rod with the desired TEM_{00} mode and thus facilitate the efficient attainment of the required 1 W of single-frequency output at 1.06 μm . This applies particularly to the design incorporating a 5-cm radius mirror which gives a beam spot radius at the rod on the order of 1.1 mm, thus giving adequate TEM_{00} mode volumes within YAG rods with nominal diameters of 3 to 5 mm. It is clear, however, that the use of such short-radius mirrors leads to tightly focused cavity geometries in the region between the radiused end of the rod and mirror R_1 , the beam-waist radius for $R_1 = 5 \text{ cm}$, being about 90 μm . Such a tight focusing of the TEM_{00} mode has led to some difficulties in obtaining stable, efficient, single-frequency operation of our Nd:YAG laser with our metallic film-tilted Fabry-Perot etalon mode filter previously used effectively in less lightly focused cavity geometries. To alleviate this problem, work during the last quarter was directed toward overcoming these difficulties encountered with the more efficient cavity designs. This effort has resulted in a major advance in the stable single-frequency techniques with the introduction of a double intracavity Fabry-Perot etalon mode filter which is less critical in adjustment and which overcomes most of the difficulties experienced with the metallic film etalon in the more sensitive, tightly focused cavities that are essential for the efficient operation of the Nd:YAG lasers. We first review the two types of two-component mode filters, together with the modifications to the cavity geometry which alleviate the stability problem in such cavities. Finally, we provide some preliminary results on the double-etalon mode filter for the stable single-frequency operation of efficient Nd:YAG lasers.

2.2 TILTED FABRY-PEROT ETALON AND METALLIC FILM MODE SELECTOR

2.2.1 Mode Filter Design and Frequency Response

The original LMSC two-component Fabry-Perot etalon and metallic film mode filter for the single-frequency operation of ND:YAG lasers is shown in Fig. 2-4. The tilted Fabry-Perot intracavity transmission etalon is tuned to the required frequency, and its selectivity is made adequate to provide the required suppression of adjacent axial modes of the particular laser cavity, the separation of which is given by $c/2L$, where L is the distance between the cavity mirrors. For Nd:YAG lasers using an efficient spherical pumping cavity ($\sim 8\text{-in. diameter}$), the axial mode spacing is around 300 MHz.

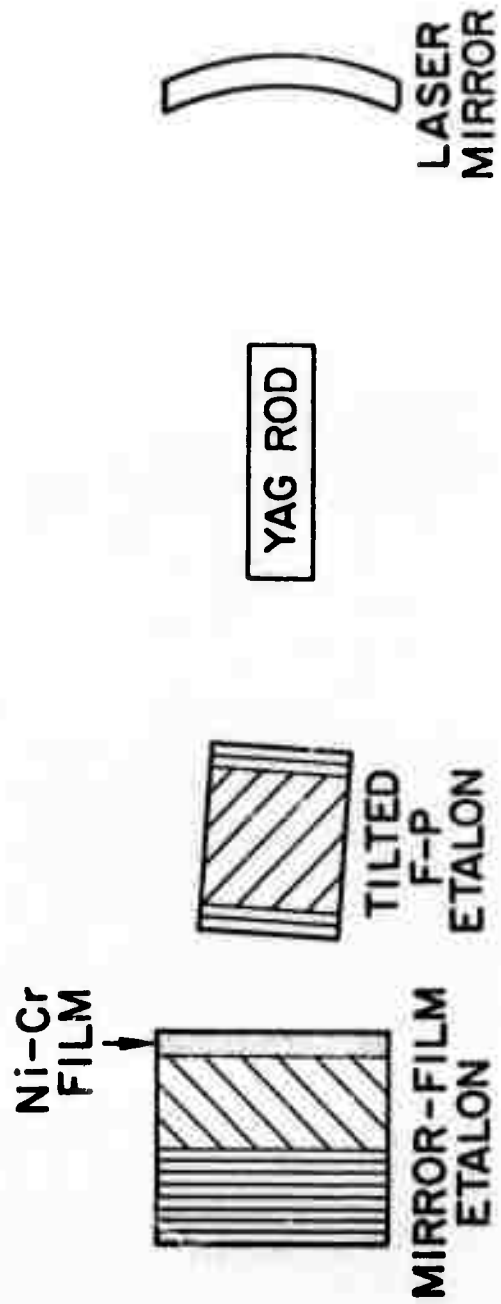


Fig. 2-4 Combination of the Tilted Fabry-Perot Etalon and the Single Metallic-Film Multilayer Reflector for Single-Frequency Operation of Nd:YAG Lasers

The function of the metallic film-mirror etalon is to suppress any oscillations at other resonances at free spectral ranges of the Fabry-Perot etalon, which are usually on the order of 10 to 20 GHz apart depending on its thickness.

Figure 2-5 shows the reflectivity versus frequency of one design of tilted Fabry-Perot etalon-metallic film mode filter which has been used to produce single-frequency Nd:YAG laser oscillations, particularly in the less highly focused cavity mode configurations. Here laser oscillation occurs at the single frequency corresponding to the main Fabry-Perot etalon response at zero on the frequency scale in the figure. The selectivity of this is made sufficient to suppress adjacent axial modes, taking into account the insertion loss and the transmission of the output mirror. The metallic film-mirror etalon is then sufficiently selective to reduce the reflectivity at other free spectral ranges of the Fabry-Perot etalon as shown and thus to allow only a single frequency of oscillation within the linewidth (\sim 150 GHz) of the Nd:YAG laser transition. Figure 2-6 shows curves of the selectivity versus frequency for an 11-mm fused quartz etalon with various reflective coatings as used in practice.

2.2.2 Discussion of Mode Filter Performance

Single-frequency power outputs of 1 W from a Nd:YAG laser when pumped at the 1-kW level by a tungsten-iodine lamp appear quite feasible using the tightly focused cavity geometries discussed earlier. Using the above Fabry-Perot etalon-metallic film mode filter with a radius R of 25 cm on one end of a 30- by 5-mm Nd:YAG rod and a 10-cm radius reflector, we have obtained 1.1-W TEM_{00} output power with a 1-kW tungsten lamp. The calculated TEM_{00} mode radius at the rod for this configuration is 0.79 mm, and hence the mode still uses only a small portion of the pumped rod. With this arrangement, a stable, single-frequency TEM_{00} output of 0.5 W has been obtained at the 1-kW pump level.

The use of a 5-cm radius reflector increases the mode radius at the rod to about 1.1 mm, which should increase the TEM_{00} output to 2 W which would then give 1 W of single-frequency output at 1.06 μm . Substantial progress has been achieved in this direction, and TEM_{00} power outputs of 2 to 2.8 W have been observed in agreement with these predictions. Some problems due to increased cavity losses and cavity

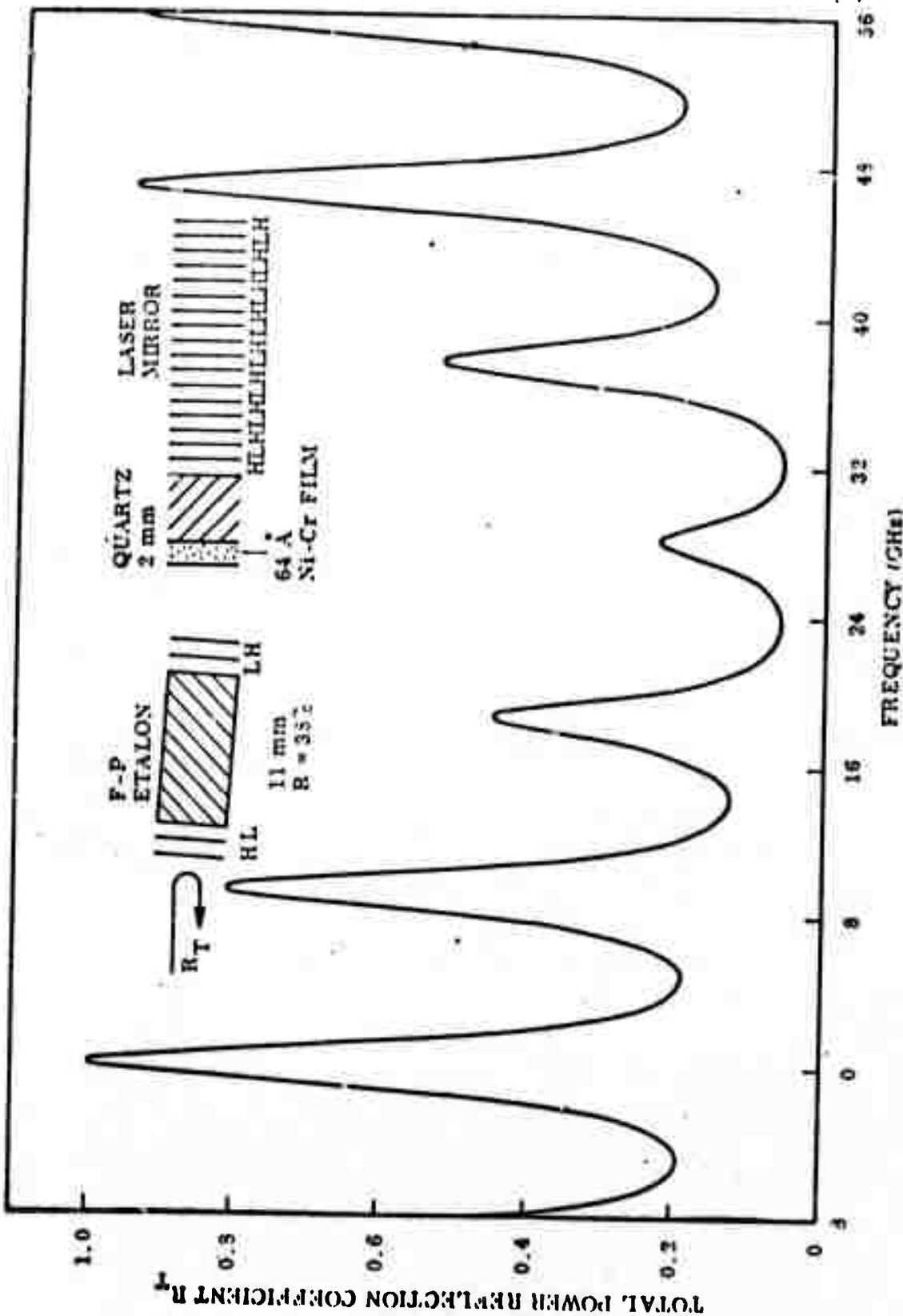


Fig. 2-5 Frequency Response for an 11-mm, 38-Percent Reflective Quartz Fabry-Perot Etalon and a 2-mm, 64 Å Nichrome Film-Laser Mirror Quartz Etalon

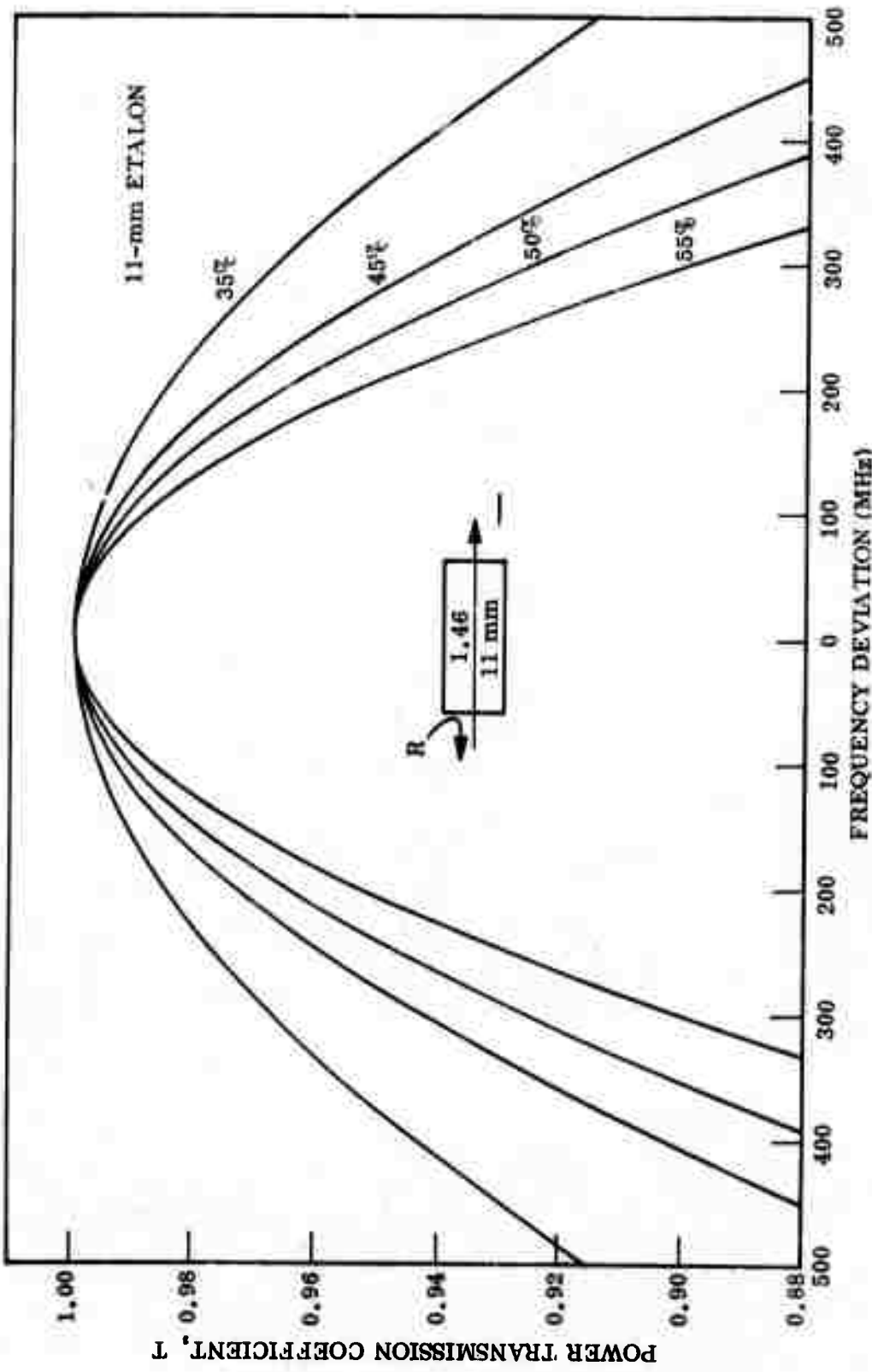


Fig. 2-6 Selectivity Curves for an 11-mm Fabry-Perot Etalon With Various Reflective Multilayer Coatings

instability have been encountered when the selective intracavity Fabry-Perot etalon is tilted to achieve single-frequency operation in such tightly focused cavity geometries. A more critical dependence on the position and insertion of the metallic film is also apparent in these more efficient, highly focused cavity designs.

These deleterious effects are due to the asymmetry introduced into the TEM_{00} mode distribution as the selective intracavity etalon is tilted, becoming more detrimental in highly focused cavity geometries. For example, in the two-dimensional case, the electric field of the TEM_{00} mode and its associated angular spectrum of plane waves at a waist position are given by

$$E_x(x) = \exp(-x^2/a^2) \quad (2.1)$$

and

$$B(k_x) = (2\pi)^{-1} a \exp(-k_x^2 a^2/4) \quad (2.2)$$

respectively, where a is the beam waist radius, and k_x is the x component of the wave vector k . The selective intracavity etalon then acts as a plane-wave filter passing waves with propagation constants appropriate to the resonance condition and the selectivity of the etalon. As the etalon is tilted, some asymmetry is introduced in the angular spectrum transmitted by the etalon which, for the more selective etalons and tightly focused cavities, leads to a mismatch of the cavity modal configuration to the fundamental TEM_{00} mode and hence to losses into higher-order transverse modes of the cavity. Such considerations were also applied in the First Semiannual Report to deduce the tilt losses of the intracavity etalon as a function of tilt angle, reflectivity, and etalon thickness, etc. It follows from such considerations that both the tilt loss and the losses due to mode mismatch will be reduced by reducing the required etalon selectivity. The reflectivity of the etalon coatings should also be reduced as far as possible consistent with obtaining the required selectivity for a given cavity length. It follows that these problems of mode selection and asymmetry will be alleviated by any modification in the cavity configuration of Fig. 2-1, which allows a reduction in the cavity length and which modifies the effect of the tilted etalon on the TEM_{00} mode distribution.

2.2.3 Use of a Convex Mirror R_1

The cavity length may be shortened by using a short radius convex mirror R_1 , which will then produce a virtual waist outside the cavity and thus allow its length to be shortened by the radius R_1 of the mirror, which maintains the same beam spot radius at the rod as obtained with the similar concave mirror R_1 . Such a modification merely changes the sign of the radius R_1 in the equations given in the First Annual Report for the deduction of the cavity TEM_{oo} mode characteristics and stability criteria. Thus, the range of stability for d_1 in Fig. 2-1 is now given by

$$d_1 = f - |R_1| \text{ to } d = f \quad (2.3)$$

and the use of a convex mirror thus shortens the required cavity configuration for a given beam spot radius at the laser rod. A further reduction in the cavity length may also be obtained with some slight reduction in the TEM_{oo} mode volume by reversing the Nd:YAG rod shown in Fig. 2-1, thus placing the rod with its curved end adjacent to the flat mirror. The combination of these two changes leads to the computed values of the spot radius W_R at the rod shown in Table 2-2 for the two-mirror radii R_1 of -10 cm and -5 cm and a flat mirror $R_2 = \infty$. These results should be compared with those shown in Table 2-1 for a concave mirror R_1 .

Table 2-2

**BEAM SPOT RADIUS W_R AT THE YAG FOR
CONVEX MIRROR RADIUS R_1 OF 5 AND 10 CM**
(All dimensions in cm; curved rod radius $R = 25$ cm)

R_1	d_1	d_2	W_R	W_o
-5	25.9	20	0.105	virtual
-10	23.3	20	0.075	virtual

2.2.4 Use of a Curved Mirror R_2

A reduction of the required cavity length, and hence of the etalon selectivity, may also be made by using a curved mirror R_2 instead of the flat mirror in the basic cavity design shown in Fig. 2-1. This has the effect of assisting the focusing effect

of the YAG rod and thus of reducing the distance d_1 . As stated already, all parameters are essentially independent of the distance d_2 which is fixed at present by the dimensions of the efficient spherical pumping cavity used in our present laser designs. The use of a curved mirror instead of the flat one also makes the laser adjustment and alignment less critical. This will produce concave TEM_{00} wave fronts at the intracavity Fabry-Perot etalon, which will increase its insertion loss slightly, depending on the mirror curvature. We may deduce the effect of the incidence of a spherical wave front on the etalon as follows. For the two-dimensional case, the curvature of the wave form changes the electric field distribution of the TEM_{00} mode to the form

$$E_x(x) = \exp(-x^2/a^2) \exp(jkx^2/2f), \quad (2.4)$$

where $R = 2f$, and R is the radius of the gaussian mode at the specific position of the etalon. The new angular spectrum of plane waves is now given by the integral

$$b'(k_x) = \frac{1}{2\pi} \int e^{-x^2/a^2} e^{-j(k_x x - kx^2/2f)} dx, \quad (2.5)$$

which may be evaluated to give

$$\begin{aligned} b'(k_x) &= \left[\frac{2}{\sqrt{\pi}} \left(1 + \frac{k^2 a^4}{4f^2} \right) \right]^{-1} a \exp \left[\frac{-k_x^2 a^2}{4 \left(1 + \frac{k^2 a^4}{4f^2} \right)} \right] \\ &\times \exp \left[j \left(\frac{1}{2} \tan^{-1} \frac{k^2 a^2}{2f} - \frac{k k_x^2 a^4}{8f \left(1 + \frac{k^2 a^4}{4f^2} \right)} \right) \right], \end{aligned} \quad (2.6)$$

where $k_x = k \sin \theta$.

Comparing Eq. (2.6) with Eq. (2.2), we see that the effective beam waist in the curved wave front may be written as

$$a' = a / \left(1 + k^2 a^4 / 4f^2 \right)^{1/2} \quad (2.7)$$

The effective beam waist corresponding to a curved wave front is thus smaller and a wider angular spectrum of plane waves is now involved, thus leading to increased insertion losses for etalons of a given selectivity. Also, because of this wider angular spectrum, the effects of asymmetry as the etalon is tilted will be different from those pertaining to the plane mirror R_2 and possibly not as severe as in the plane mirror geometry. Such a modification to the basic cavity design was investigated during the present reporting period.

Some results on the TEM_{00} mode parameters for various radii R_2 of the curved mirror are given in Table 2-3. These should be compared with those given in Table 2-1 for the flat mirror R_2 .

Table 2-3
BEAM SPOT RADIUS AT THE YAG ROD AND BEAM WAIST
FOR VARIOUS CURVED LASER MIRROR RADII R_1 AND R_2
(Curved rod radius $R = 25$ cm; all dimensions in cm)

R_1	R_2	d_1	d_2	$\frac{W}{R}$	$\frac{W_o}{R}$
5	400	30.3	20	0.1029	0.0092
5	200	28.3	20	0.0951	0.0092
5	100	26.1	20	0.0837	0.0092
5	60	19.3	20	0.0625	0.0092
10	400	32.7	20	0.0731	0.0130
10	200	30.5	20	0.0677	0.0130
10	100	26.5	20	0.0576	0.0130
10	60	21.7	20	0.0451	0.0130

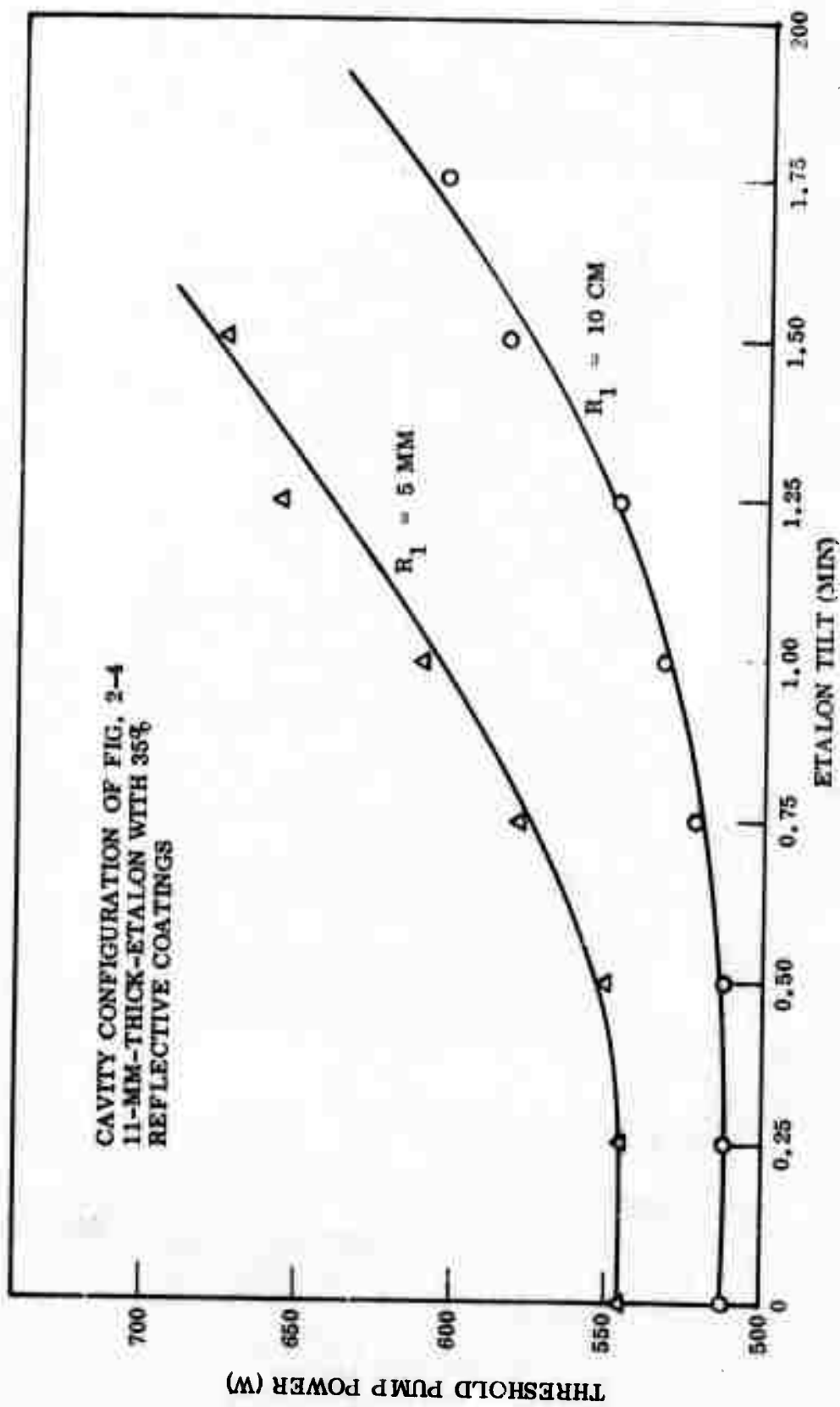
The cavity length may thus be reduced with such a curved mirror R_2 without seriously affecting the TEM_{00} mode volume in the rod for mirror radii equal or greater than 200 cm. Furthermore, the use of such a curved mirror helps to decouple the intra-cavity etalon from the laser mirror, thus reducing the tilt angle required for adequate decoupling. The effect of such converging wave fronts on the tilt loss of the etalon have also been computed, and values for the mirror radius R_2 for use in experimentation have been established.

2.2.5 Etalon Loss in Highly Focused Laser Cavities

Some experimental results on the observed increase in the threshold pump power as a function of etalon tilt angle for the cavity configuration shown in Fig. 2-4 are given in Fig. 2-7. These curves were obtained with only the selective etalon in the laser cavity, i.e., no metallic film, and a 2-percent transmission output mirror. The insertion loss of the tilted etalon may be deduced from these curves; we can clearly see the increase in the insertion loss as the cavity-mode focusing is made tighter; e.g., when going from a 10- to a 5-cm radius mirror R_1 . Thus, for a tilt angle of $1 \text{ } \widehat{\text{min}}$, we calculate an etalon insertion loss of 0.2 percent and 0.6 percent for cavity configurations that use a 10- and a 5-cm radius mirror, respectively. Also, it is possible to obtain single-frequency operation with tilt angles of less than $1 \text{ } \widehat{\text{min}}$. However, the etalon is then not sufficiently decoupled from the flat end mirror of the cavity, and the laser at that time is very sensitive to mechanical perturbations.

The replacement of the flat mirror with a long-radius curved mirror R_2 as discussed in the previous section greatly reduces the sensitivity to alignment and also effects further decoupling of the etalon from the end mirror. We have operated our Nd:YAG lasers with mirrors of radii $R_2 = 4, 2, \text{ and } 1.2 \text{ m}$ and have essentially verified the calculated results summarized in Table 2-3.

The insertion loss of the etalon was observed to increase more slowly with increasing tilt angle in cavity configurations using a curved mirror R_2 than in those using a flat mirror, although a small loss is now observed even for no tilt. Figure 2-8 shows the threshold pump power as a function of tilt angle for mirror radii R_2 of 4 m and 1.2 m and a mirror R_1 of radius 5 cm. These curves cannot be directly compared with those



2-15

Fig. 2-7 Threshold Pump Power of Nd:YAG Laser Versus Intracavity Fabry-Perot Etalon Tilt Angle for an 11-mm Quartz Etalon with 35-Percent Reflective Coatings

CAVITY CONFIGURATION OF FIG. 2-4 EXCEPT
FLAT HR END MIRROR REPLACED BY 4 M AND
1.2 M RADIUS MIRRORS. $R_1 = 5$ CM.
11-MM-THICK TILTED ETALON WITH 45%
REFLECTIVE COATINGS

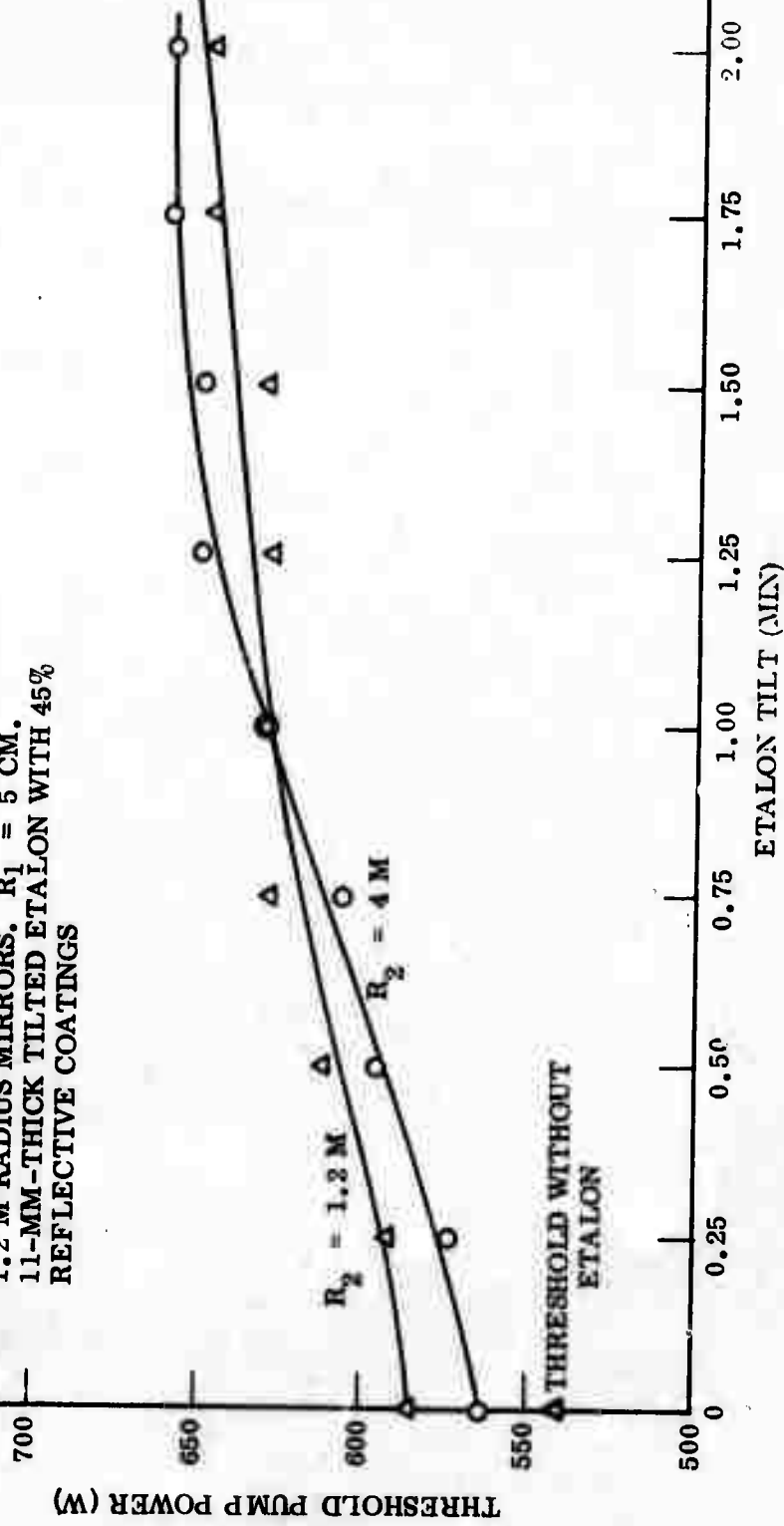


Fig. 2-8 Flat Laser Mirror Replaced by a Curved Mirror. Threshold pump power of Nd:YAG laser versus tilt angle for an 11-mm quartz intracavity etalon with 45-percent reflective coatings

in Fig. 2-7 because a more selective etalon with 45-percent reflective coatings was used in the data given in Fig. 2-8. However, the decreased sensitivity of the variation of the threshold with tilt angle is very evident in the results obtained with the curved mirrors R_2 . We are presently evaluating such cavity designs using a long-radiusied mirror R_2 instead of the flat mirror for the final design of a stable, single-frequency Nd:YAG laser.

2.2.6 Conclusions

It thus appears that the use of a curved mirror R_2 would alleviate the increase in insertion loss as the main selective Fabry-Perot intracavity etalon is tilted in highly focused cavity geometries. This would then require the use of a curved mirror-metallic film etalon to suppress laser oscillations at other free spectral ranges of selective Fabry-Perot etalon. This is quite possible to accomplish, and our tilted Fabry-Perot etalon-metallic film mode film could be made to operate quite satisfactorily in such highly focused laser cavity designs. Such a procedure is not too satisfactory, however, and, in addition, the metallic film seems to make the laser more sensitive to alignment and less stable than is desirable for systems applications. Such matters are still under consideration, but it would appear that a very advantageous change resulting from work done during this reporting period is to substitute a thin, low-reflectivity second dielectric intracavity etalon for the metallic film to perform the same filtering function.

2.3 DOUBLE-INTRACAVITY ETALON MODE FILTER

One arrangement of the double Fabry-Perot etalon mode filter for the single-frequency operation of Nd:YAG lasers is shown in Fig. 2-9. During this quarter, analysis on this arrangement has been initiated. Preliminary results indicate that substantial improvement in the overall stability and ease of adjustment for the operation of the single-frequency laser is obtainable. However, a comprehensive presentation of the theory is deferred to the next quarter since there still are some fine details to be completed.

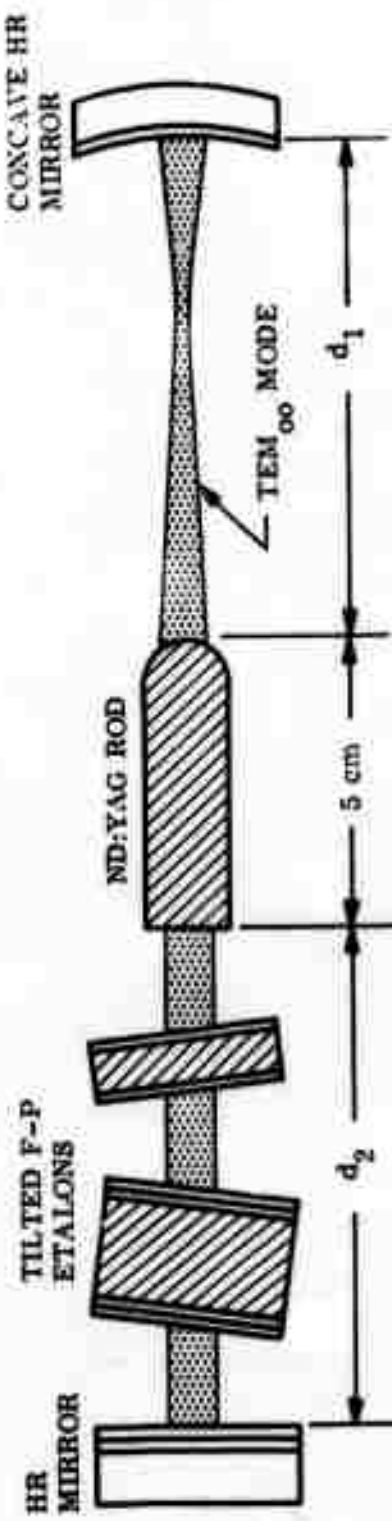


Fig. 2-9 Double Intracavity Fabry-Perot Etalon Mode Filter for the Single-Frequency Operation of Nd:YAG Lasers

2.4 PLANS FOR NEXT QUARTER

During the next quarter, efforts will be directed toward a detailed investigation of the performance of the new double-intracavity Fabry-Perot etalon mode filter.

Particular attention will be given to questions such as the case of attaining single-frequency oscillations in efficient Nd:YAG lasers, the single-frequency power output attainable with tungsten-iodine and potassium-rubidium lamps, and the efficiency.

To alleviate the etalon selectivity requirements, short radius convex mirrors will be used to obtain the necessary TEM_{00} mode volume in the laser rod for efficient operation, and the cavity length will thus be reduced. Somewhat longer radius mirrors (~ 2 m) will also be used instead of the normally flat mirror at the other end of the laser. This will assist the focusing as performed by the laser rod and lead to less critical effects when the tilted etalon is inserted.

Work will continue on the efficient use of the potassium-rubidium lamp with improvements in the lamp design for longer lifetimes and also in the operation of the single-frequency Nd:YAG laser with such lamps in dielectric-coated pump cavities.

Section 3

WIDE BANDWIDTH ELECTROOPTICAL MODULATOR

3.1 MEASUREMENT TECHNIQUES FOR 2- to 4-GHz MODULATION

In the Fifth Quarterly Report, various techniques that are applicable to the measurement of modulation index in the 2- to 4-GHz band were indicated. In the Second Semiannual Report, calibration of a TIXL Avalanche photodiode for use in this frequency range was reported. During the past quarter, additional work on the theory of sideband power measurements was done. A comprehensive presentation of the analysis of the sideband-power measurement techniques and their limitations is given in this section.

Analysis of Sideband-Power Measurements. In a birefringent modulator, the input light beam is polarized at 45 deg to the two birefringent axes (the e- and the o-axes) of the electrooptic crystal. The beam propagates down the other o-axis of the crystal and interacts with an applied rf E-field through its action on the crystal refractive indexes. Thus, the situation is as depicted in Fig. 3-1, in which the coordinate system, crystal axes, and refractive indexes used in the analysis are shown. The input light beam is designated by the optical E-field, E_o , having components $E_x = E_y$ along the birefringent axes.

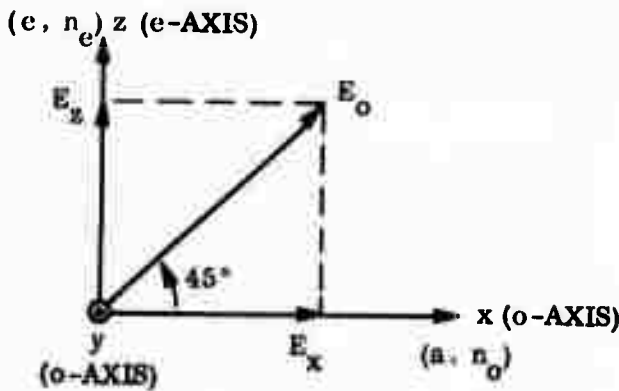


Fig. 3-1. Coordinate-System, Crystal Axes and Input Light Polarization Used for the Sideband Power Analysis

At the output of the modulating crystal of length ℓ , then,

$$E_x = \frac{E_o}{\sqrt{2}} \exp \left[-j \beta_o \ell \left(n_o - \Delta n_o \sin \omega_M t \right) \right] \exp (j \omega_o t) \quad (3.1)$$

$$E_z = \frac{E_o}{\sqrt{2}} \exp \left[-j \beta_o \ell \left(n_e - \Delta n_e \sin \omega_M t \right) \right] \exp (j \omega_o t) \quad (3.2)$$

where

$$\beta_o = \frac{\omega_o}{c}, \quad \omega_o = \text{optical frequency}$$

n_o, n_e = ordinary and extraordinary indexes, respectively

$\Delta n_o, \Delta n_e$ = change of refractive indexes due to the modulation field of peak value E_{zM}

ω_M = modulation frequency

For LiNbO₃

$$\left\{ \begin{array}{l} \Delta n_o = \frac{n_o^3}{2} r_{13} E_{zM} \\ \Delta n_e = \frac{n_e^3}{2} r_{33} E_{zM} \end{array} \right\}, \text{ where } r_{13} \text{ and } r_{33} \text{ are the appropriate EO coefficients.}$$

After passing through the compensator which imparts static phase retardations of ϕ_x and ϕ_z to the o- and e-rays, respectively, the orthogonal components E_x and E_y are given by:

$$E_x = \frac{E_o}{\sqrt{2}} \exp \left[-j \theta_o \left(n_o - \Delta n_o \sin \omega_M t \right) \right] \exp (j \omega_o t) \exp (-j \phi_x) \quad (3.3)$$

$$E_z = \frac{E_o}{\sqrt{2}} \exp \left[-j \theta_o \left(n_e - \Delta n_e \sin \omega_M t \right) \right] \exp (j \omega_o t) \exp (-j \phi_z) \quad (3.4)$$

where

$$\theta_o = \beta_o l$$

Therefore, after the compensator, the optical E-field along the 45-deg line, E_t , is given by:

$$\begin{aligned} E_t &= \frac{E_x}{\sqrt{2}} + \frac{E_z}{\sqrt{2}} \\ &= \frac{E_o}{2} \exp (j \omega_o t) \left\{ \exp \left[-j \left(\phi_x + n_o \theta_o - \Delta n_o \theta_o \sin \omega_M t \right) \right] \right. \\ &\quad \left. + \exp \left[-j \left(\phi_z + n_e \theta_o - \Delta n_e \theta_o \sin \omega_M t \right) \right] \right\} \\ &= \frac{E_o}{2} \exp (j \omega_o t) \left\{ \exp (-j \phi_o) \exp (j X_o \sin \omega_M t) + \exp (-j \phi_e) \exp (j X_e \sin \omega_M t) \right\} \end{aligned} \quad (3.5)$$

where

$$\phi_o = \phi_x + n_o \theta_o, \quad \phi_e = \phi_z + n_e \theta_o,$$

$$X_o = \Delta n_o \theta_o, \quad X_e = \Delta n_e \theta_o$$

In other words, if an analyzer is aligned at the output to this 45-deg line, the optical E-field after passing through the analyzer will be given by Eq. (3.5).

Let $\epsilon_t = \frac{E_t}{E_o/2}$ normalized field after passing through the analyzer, Eq. (3.5) then may be rewritten as:

$$\epsilon_t = e^{j(\omega_o t - \phi_o)} e^{jX_o \sin \omega_M t} + e^{j(\omega_e t - \phi_e)} e^{jX_e \sin \omega_M t} \quad (3.6)$$

In general,

$$\begin{aligned} e^{jX \sin \omega_M t} &= \sum_{-\infty}^{\infty} J_n(X) e^{jn\omega_M t} \\ &= J_0(X) + J_1(X) e^{j\omega_M t} + J_{-1}(X) e^{-j\omega_M t} \\ &\quad + J_2(X) e^{j2\omega_M t} + J_{-2}(X) e^{-j2\omega_M t} \\ &\quad + J_3(X) e^{j3\omega_M t} + J_{-3}(X) e^{-j3\omega_M t} \\ &\quad + \dots \end{aligned} \quad (3.7)$$

and

$$J_{-n}(X) = (-1)^n J_n(X) \quad (3.8)$$

$$\begin{aligned}
 \therefore E_t = & e^{j(\omega_0 t - \phi_0)} \left\{ J_0(X_0) + J_1(X_0) e^{j\omega_M t} - J_1(X_0) e^{-j\omega_M t} \right. \\
 & + J_2(X_0) e^{j2\omega_M t} + J_2(X_0) e^{-j2\omega_M t} \\
 & + J_3(X_0) e^{j3\omega_M t} - J_3(X_0) e^{-j3\omega_M t} \\
 & + \dots \left. \right\} \\
 & + e^{j(\omega_0 t - \phi_e)} \left\{ J_0(X_e) + J_1(X_e) e^{j\omega_M t} - J_1(X_e) e^{-j\omega_M t} \right. \\
 & + J_2(X_e) e^{j2\omega_M t} + J_2(X_e) e^{-j2\omega_M t} \\
 & + J_3(X_e) e^{j3\omega_M t} - J_3(X_e) e^{-j3\omega_M t} \\
 & + \dots \left. \right\} \quad (3.9)
 \end{aligned}$$

Regrouping terms, therefore,

$$\begin{aligned}
 \hat{\epsilon}_t = & \left[J_0(X_o) e^{-j\phi_o} + J_0(X_e) e^{-j\phi_e} \right] e^{j\omega_o t} && \text{carrier} \\
 & + \left[J_1(X_o) e^{-j\phi_o} + J_1(X_e) e^{-j\phi_e} \right] e^{j(\omega_o + \omega_M)t} && \text{first-order USB} \\
 & - \left[J_1(X_o) e^{-j\phi_o} + J_1(X_e) e^{-j\phi_e} \right] e^{j(\omega_o - \omega_M)t} && \text{first-order LSB} \\
 & + \left[J_2(X_o) e^{-j\phi_o} + J_2(X_e) e^{-j\phi_e} \right] e^{j(\omega_o + 2\omega_M)t} && \text{second-order USB} \\
 & + \left[J_2(X_o) e^{-j\phi_o} + J_2(X_e) e^{-j\phi_e} \right] e^{j(\omega_o - 2\omega_M)t} && \text{second-order LSB} \\
 & + \left[J_3(X_o) e^{-j\phi_o} + J_3(X_e) e^{-j\phi_e} \right] e^{j(\omega_o + 3\omega_M)t} && \text{third-order USB} \\
 & - \left[J_3(X_o) e^{-j\phi_o} + J_3(X_e) e^{-j\phi_e} \right] e^{j(\omega_o - 3\omega_M)t} && \text{third-order LSB} \\
 & \vdots && \\
 & + \dots &&
 \end{aligned} \tag{3.10}$$

where

USB and LSB indicate upper and lower sidebands, respectively,

or

$$\begin{aligned}
 \hat{\epsilon}_t = & \sum_{o=0}^{\infty} \left[J_n(X_o) e^{-j\phi_o} + J_n(X_e) e^{-j\phi_e} \right] e^{j(\omega_o + n\omega_M)t} \\
 & + \sum_{n=1}^{\infty} (-1)^n \left[J_n(X_o) e^{-j\phi_o} + J_n(X_e) e^{-j\phi_e} \right] e^{j(\omega_o - n\omega_M)t} \\
 & = \sum_{o=0}^{\infty} \hat{\epsilon}_{t,n} + \sum_{n=1}^{\infty} (-1)^n \hat{\epsilon}_{tn}
 \end{aligned} \tag{3.11}$$

where

- $\hat{\epsilon}_{to}$ = Optical E-field of the carrier, and
- $\hat{\epsilon}_{tn}$ = Optical E-field of the n^{th} order sideband.

Equation (3.11) gives the normalized total optical E-field, after leaving the modulator compensator and analyzer, in terms of the carrier field and the sideband fields of various orders. In an actual measurement, \hat{E}_t is directed to a scanning Fabry-Perot interferometer. The action of the scanning interferometer is to filter out power at one optical frequency (e.g., the carrier or any sideband frequency) at a time that the resonant frequency of the interferometer is swept through its tuning range. That is, at the time that the resonant frequency of the interferometer is coincident with a sideband frequency, the intensity of that sideband is transmitted and detected by the photodetector.

Therefore, the normalized carrier power P_c is given by $1/2 \hat{E}_{to} \hat{E}_{to}^*$, where the asterisk indicates the complex conjugate, or,

$$\begin{aligned} P_c &= \frac{1}{2} \left[J_0(X_o) e^{-j\phi_o} + J_0(X_e) e^{-j\phi_e} \right] \left[J_0(X_o) e^{j\phi_o} + J_0(X_e) e^{j\phi_e} \right] \\ &= \frac{1}{2} \left\{ [J_0(X_o)]^2 + [J_0(X_e)]^2 + J_0(X_o) J_0(X_e) \left[e^{j(\phi_o - \phi_e)} + e^{-j(\phi_o - \phi_e)} \right] \right\} \\ &= \frac{1}{2} \left\{ [J_0(X_o)]^2 + [J_0(X_e)]^2 \right\} + J_0(X_o) J_0(X_e) \cos(\phi_o - \phi_e) \end{aligned} \quad (3.12)$$

The first-order USB

$$P_{1+} = \frac{1}{2} \hat{E}_{t_1} \hat{E}_{l_1}^* \quad (3.13)$$

or

$$P_{1+} = \frac{1}{2} \left\{ [J_1(X_o)]^2 + [J_1(X_e)]^2 \right\} + J_1(X_o) J_1(X_e) \cos(\phi_o - \phi_e) \quad (3.14)$$

Clearly,

$$\begin{aligned} P_{n+} &= \frac{1}{2} \left\{ [J_n(X_o)]^2 + [J_n(X_e)]^2 \right\} \\ &\quad + J_n(X_o) J_n(X_e) \cos(\phi_o - \phi_e) \end{aligned} \quad (3.15)$$

and

$$P_{n+} = P_{n-} \text{ (i.e., USB power} = \text{ LSB power)} \quad (3.16)$$

Therefore, the ratio of sideband to carrier power is given by:

$$\frac{P_n}{P_c} = \frac{\left[J_n(X_o) \right]^2 + \left[J_n(X_e) \right]^2 + 2 J_n(X_o) J_n(X_e) \cos (\phi_o - \phi_e)}{\left[J_o(X_o) \right]^2 + \left[J_o(X_e) \right]^2 + 2 J_o(X_o) J_o(X_e) \cos (\phi_o - \phi_e)} \quad (3.17)$$

where

$$\begin{aligned} \phi_o - \phi_e &= \phi_x + n_o \beta_o l - (\phi_y + n_e \beta_e l) \\ &= \text{static optical bias of the modulator, and can be adjusted by varying} \\ &\text{the static birefringence angle (thickness) of the compensator, } \phi_x \\ &\text{and } \phi_y. \end{aligned}$$

Equations (3.12), (3.15), and (3.17) give the carrier power, the sideband power, and their ratios as a function of optical bias ($\phi_o - \phi_e$) and electrooptic retardation angles X_e and X_o . Since these are transcendental equations, the simplest solutions are obtained by means of numerical analysis. The analysis can be made by assuming a particular crystal, e.g., LiNbO_3 , so that the relationship between X_o and X_e is known through the published electrooptic coefficients r_o and r_e , viz.,

$$\frac{X_o}{X_e} = \frac{\Delta n_o}{\Delta n_e} = \frac{n_o^3 r_o E_{zM}}{n_e^3 r_e E_{zM}} = \text{constant A} \quad (3.18)$$

where r_o and r_e are the electrooptic coefficients along the o- and the e-axis, respectively. Or, if the ratio A between X_o and X_e is desired for a particular crystal, a simple measurement can readily be made using the same setup for sideband power measurements. Efforts along these directions will be continued next quarter.

3.2 MODULATION TESTS

Tests on modulation index continued during this quarter. Unfortunately, because of a mechanical problem within the modulator, the 5-mm LiNbO_3 crystal used in the last quarter was broken off early in the quarter. An 8-mm LiNbO_3 crystal was used instead. This was also planned for this quarter since a crystal of this length should give a much higher modulation index for a given drive power if no other problems were encountered.

Figure 3-2 shows the results of the first tests using the long crystal. At an rf drive level of 10W, only an average of 25-percent modulation index was obtained after the modulator had been "properly" tuned for the crystal. In addition, beam distortion due to rf heating effects was observed, especially at the high-frequency end (3.6 to 4.0 GHz). When the drive power was dropped down to 4W, heating effect was nonobservable, but the modulation index was only 15 percent.

Separate runs were made at an rf drive level of 5W, and over a large portion of the 2- to 4-GHz band, a modulation index of 25 percent was obtained. A typical curve is shown in Fig. 3-3. Unfortunately, the index drops off at both high- and low-frequency ends so that the 3-dB bandwidth is somewhat less than 2 GHz. Although the results for 5-W drive level using this 8-mm crystal were comparable to those obtained last quarter for a 5-mm crystal, the modulator performance is still worse because: (1) it should give an increase in modulation index of approximately 1.6 (the ratio of 8 to 5); and (2) its bandwidth is reduced from the original 2 GHz.

A further check is made with the drive power flow in the reverse direction. Two tests were run: one with the output terminated in a $50-\Omega$ load; the other, with output shorted.

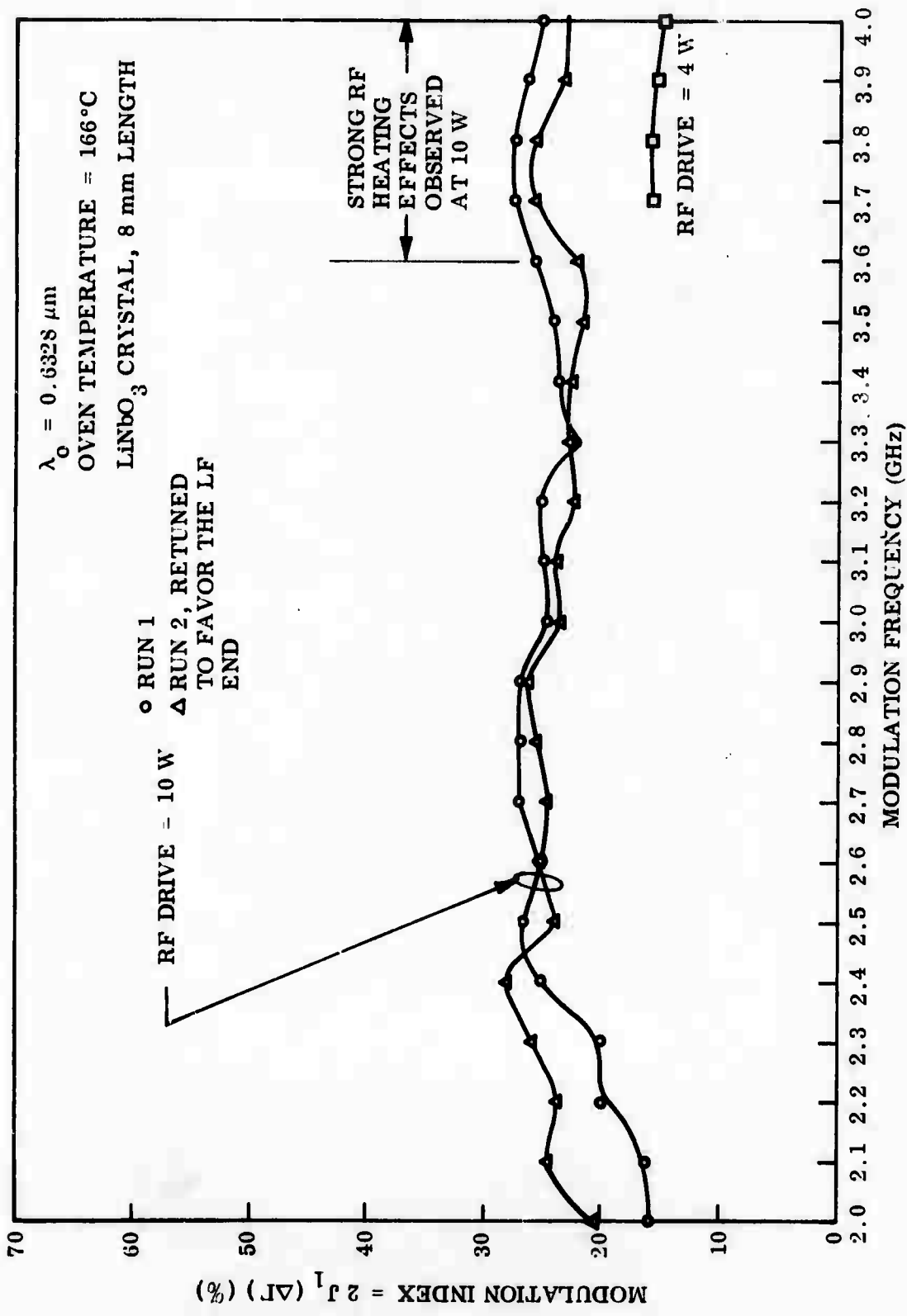


Fig. 3-2 Modulation Index Versus Frequency for Various rf Drive Levels

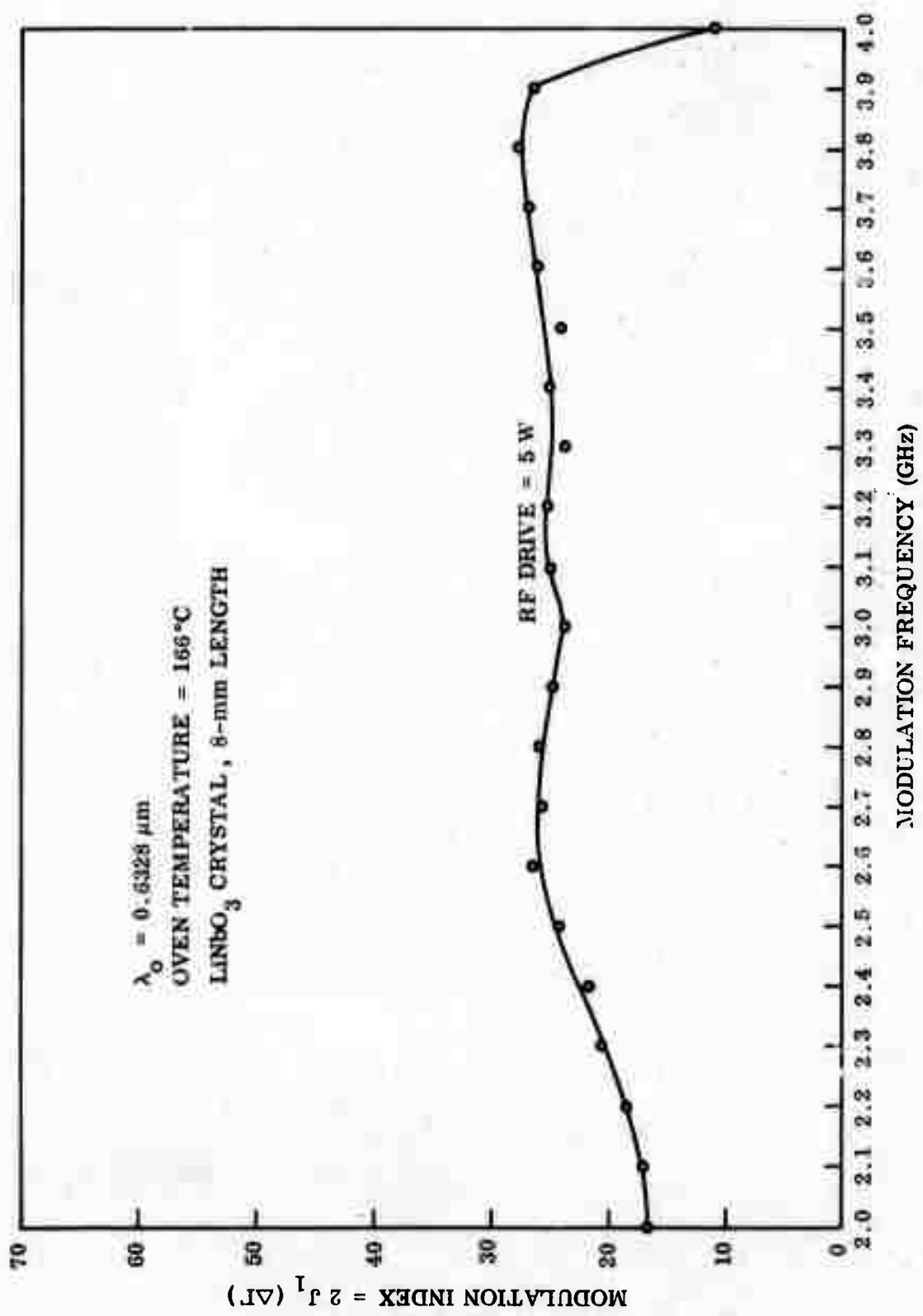


Fig. 3-3 Modulation Index Versus Frequency at 5-W rf Level

The one with the output terminated showed less modulation index and 3-dB bandwidth than the run made last quarter under similar conditions but with a 5-mm crystal. The one having a shorted output showed a highly nonuniform rf field; the modulation index versus frequency curve was essentially in two lobes — there was no response higher than 3.5 GHz. These curves are shown in Fig. 3-4.

The results of these tests were rather discouraging because they appeared to show that longer crystals were not suitable. However, they could also indicate that the problems were associated with the particular crystal itself. Thus, another crystal was substituted. It was then found that there was rather poor contact between the crystal and the electrodes. This could at least account for part of the problems.

A new crystal was substituted, and care was exercised to clean off the electrodes to ensure best contact. Test runs were made at 0.5145 μ m. The results were considerably more encouraging, as shown in Figs. 3-5 and 3-6.

Figure 3-5 gives the results of modulation index measurements for both 10-W and 5-W drive levels. No rf heating problem was observed — this was most encouraging — although the modulation index obtained was still much less than what it should be. Figure 3-6 shows the modulation index obtained for the same arrangement but using the usual birefringence sideband measurement method. The modulation index so calculated for 5-W drive is much higher than that shown in Fig. 3-6, although the shape is still the same. The reason for this discrepancy is not yet clear and will be investigated further next quarter.

It should be noted that the rf drive levels indicated in the above tests were those measured at a power meter which is separated from the modulator by a directional coupler, a cable, and adapters. Therefore, the actual power at the modulator is somewhat less than the indicated power. Figure 3-7 shows the actual power measured at the input to the modulator for an indicated power level of 5 W. It is seen that only approximately 4W was delivered to the modulator. Scaling, these results correspond to about 15 W of

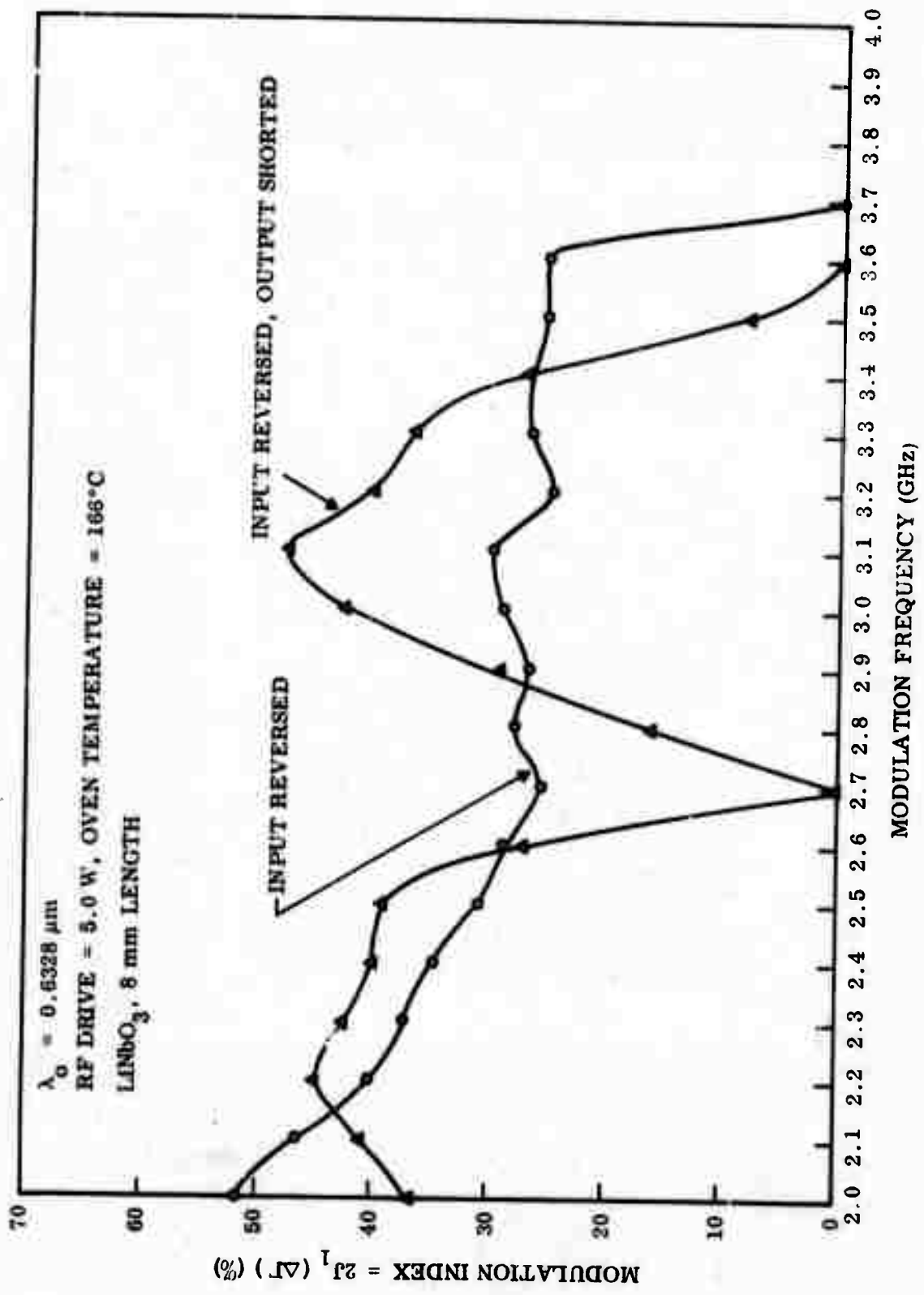


Fig. 3-4 Modulation Index Versus Frequency With rf Power Flow in the Reverse Direction

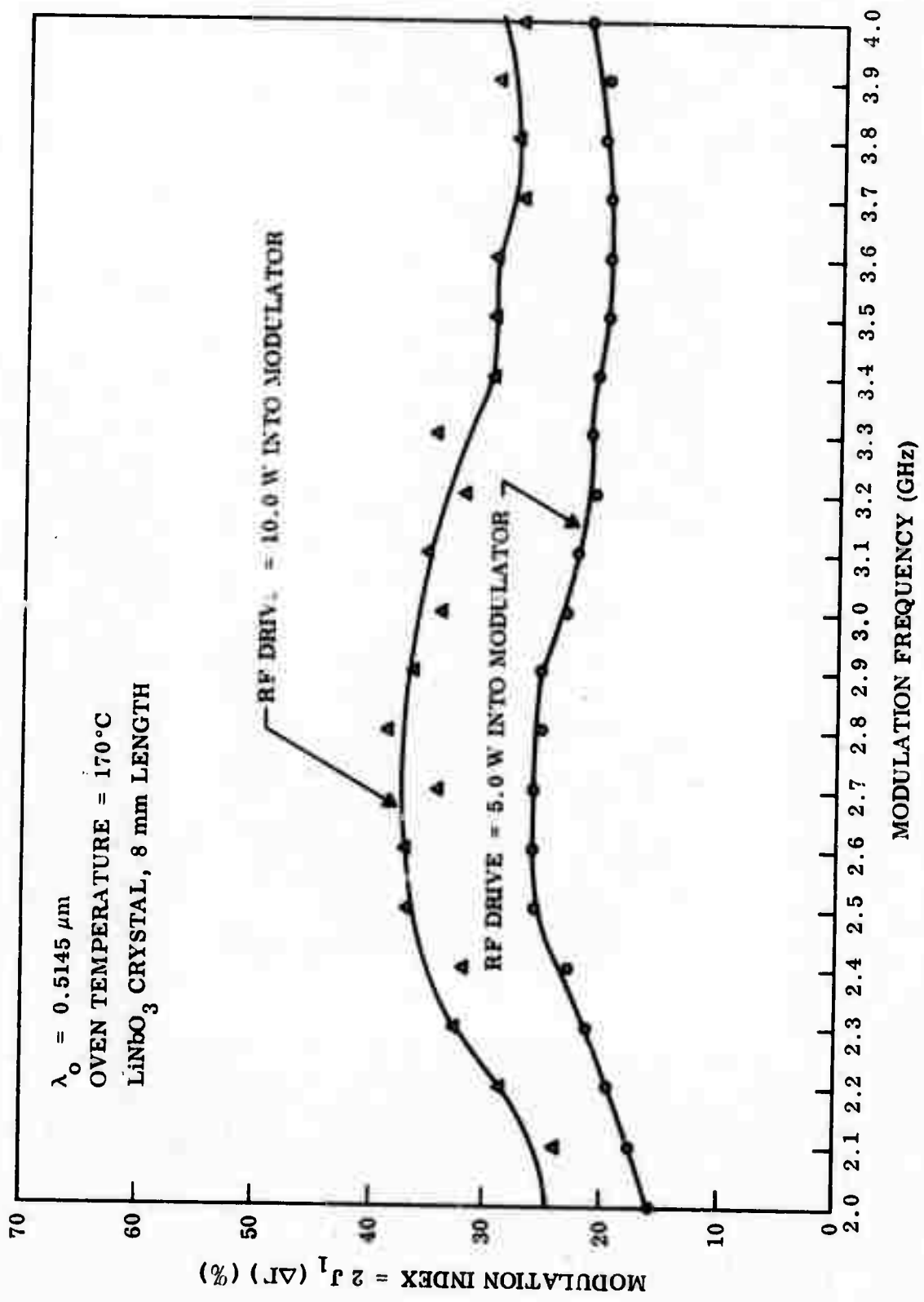


Fig. 3-5 Modulation Index Versus Frequency at Various Power Levels, Calculated From the Sideband of the Extraordinary Ray Only

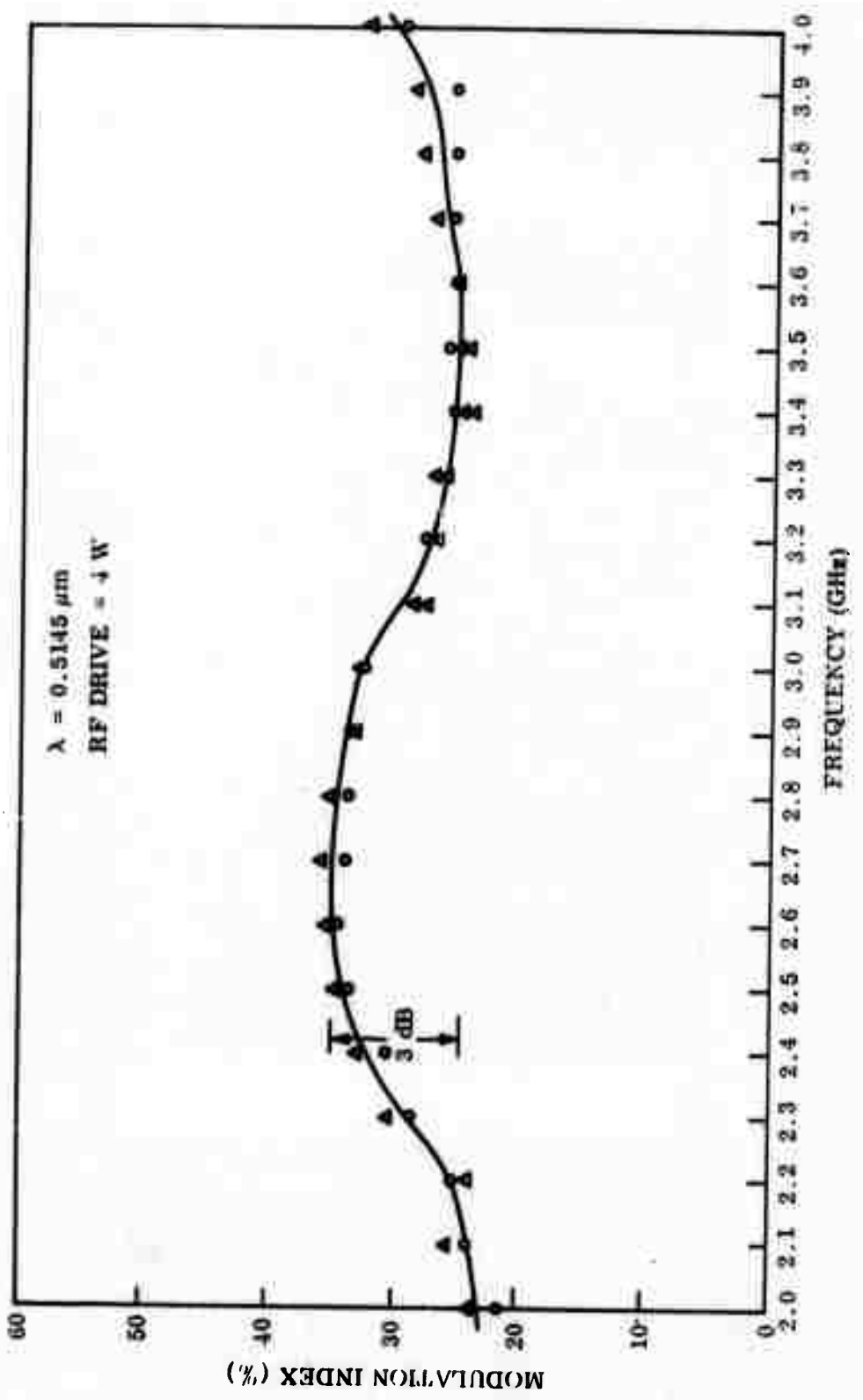


Fig. 3-6 Modulation Index Versus Frequency for 8-mm LiNbO_3 Crystal Using the Birefringent Sideband Measurement

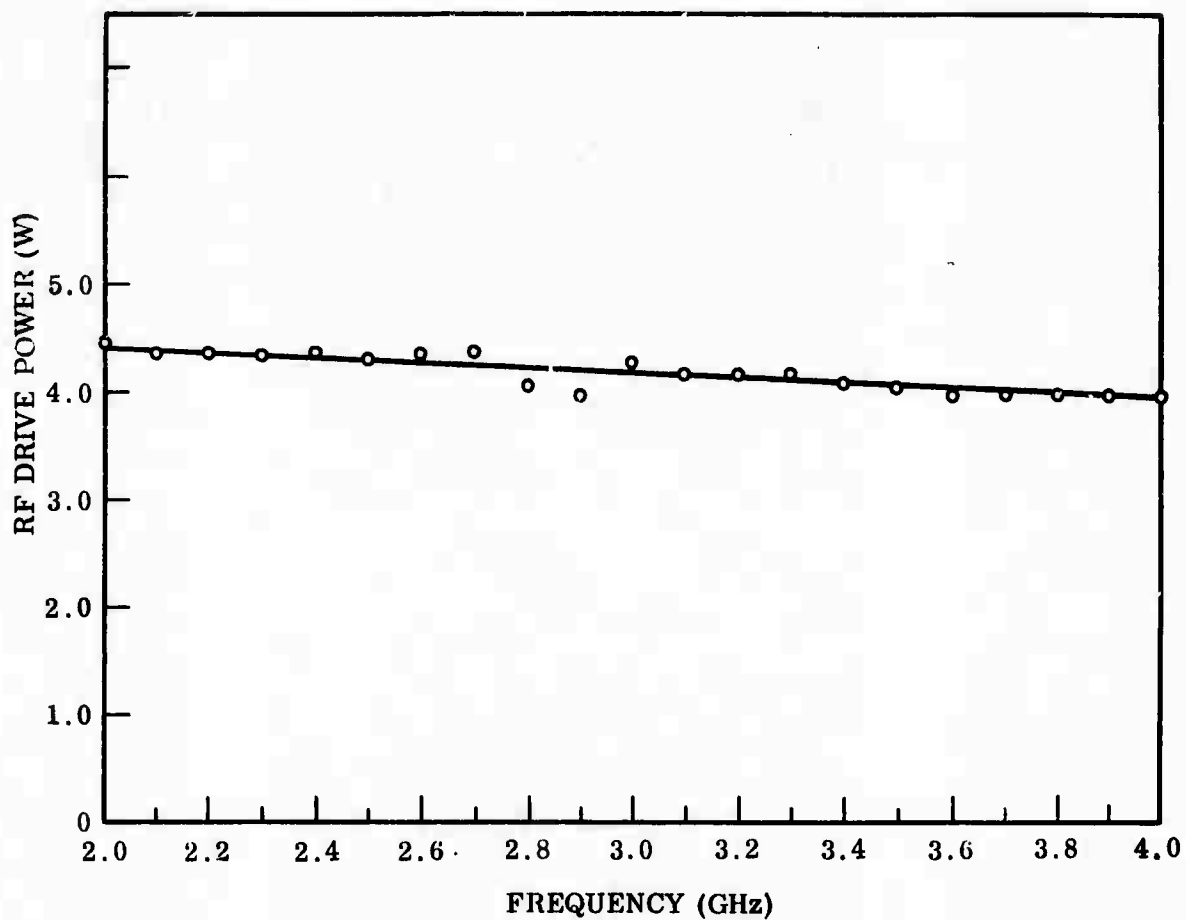


Fig. 3-7 Actual rf Drive Power Into the Modulator as a Function of Frequency

rf drive power to obtain 33-percent modulation index at 1.06 μm . Clearly, these results are worse than those obtained last quarter. Part of this degradation in performance is due to the fact the crystal was too long for the modulator circuit.

3.3 FUTURE PLANS

During the next quarter, additional analysis will be performed. Further tests on this modulator in its present form will be made. Specifically, the discrepancy between the measurements will be resolved. The contact and subsequent heating problems will be investigated. If the 8-mm crystal proves to be too long for this modulator, shorter crystals will be used. Finally, tests at 1.06 μm will be made.